PERC-based shingled solar cells and modules at Fraunhofer ISE

Puzant Baliozian, Nils Klasen, Nico Wöhrle, Christoph Kutter, Hannah Stolzenburg, Anna Münzer, Pierre Saint-Cast, Max Mittag, Elmar Lohmüller, Tobias Fellmeth, Mohammad Al-Akash, Achim Kraft, Martin Heinrich, Armin Richter, Andreas Fell, Alma Spribille, Holger Neuhaus & Ralf Preu, Fraunhofer Institute for Solar Energy Systems ISE, Freiburg, Germany

Abstract

Achieving high output power densities p_{out} of silicon-based PV modules requires an increase of cell efficiency as well as a reduction of cell-to-module (CTM) losses. Solar cell shingling, an approach first introduced in the 1950s, targets the reduction of CTM losses mainly by: 1) eliminating the cell spacing through the overlapping of neighbouring cells; 2) decreasing the shading losses by covering the busbar with a neighbouring cell's active area; and 3) reducing the series resistance losses at the interconnection level. This paper reports on the latest advances in passivated emitter and rear cell (PERC)-based shingled solar cell activities at Fraunhofer ISE. The approach taken is to fabricate 6" host wafers from Czochralski-grown silicon and separate them after metallization and contact firing into bifacial p-type shingled passivated edge, emitter and rear (pSPEER) solar cells. The separation is performed by laser-assisted processes: 1) laser scribing and mechanical cleaving, or 2) thermal laser separation. Since the separation process leaves the edges without the intended passivation, high edge recombination rates are expected. For that reason, a photoluminescence-based method to characterize edge recombination has been developed and verified by Quokka3 simulations. In order to further increase the pSPEER output power density p_{out} for a cell without the intended edge passivation, a post-metallization/separation edge passivation method, i.e. Passivated Edge Technology (PET), has been developed. The implementation of PET in pSPEER^{PET} solar cells leads to an enhanced designated area p_{out} = 23.5mW/cm^2 (considering an additional rear-side irradiance G_r = 100W/m^2). In the transition to shingled-module assembly, the study follows up with the cure kinetics of electrically conductive adhesives (ECAs) and mechanical-model-based methods to gain a better understanding of the joint between pSPEER cells within strings. A CTM analysis using the SmartCalc.CTM software shows a comparison of a parallel-stringing topology with a matrix topology of the cell interconnection. The reduced form factor of shingled solar cells makes them very appealing and effective for use in integrated module products, which is demonstrated by a successful automotive application, additionally profiting from the high p_{out} attained. Drawing from the authors' expertise in customized module and surface design, a vehicle-integrated PV solution with a highly aesthetic appearance is presented.

Introduction

Just two years after the first fabricated silicon-based solar cell [1], the shingled interconnection of solar cells was introduced in a 1956-filed patent (see Fig. 1(a)) [2]. Subsequently, numerous patents were filed for various applications, such as satellite solar cell arrays [3], different interconnection patterns/ geometries, and thermally stable shingle arrays [4]. Early publications, including results for shingled solar cells, target 1) low-illumination applications in electronic devices [5]; and 2) prototype vehicles with limited power-generation areas [6].

Commercial modules with shingled solar cells are currently available on the market [7,8], with a projection trend indicating an increasing market share in the upcoming years [9]. The recent patents (see the example in Fig. 1(b) [10,11], as well as reports in the literature [12–15]) highlight the increase in research activities relating to the shingling concept. Shingling is a process whereby neighbouring cells are mechanically and electrically interconnected by overlapping the rear-side busbar of one cell with the following neighbouring cell's front-side busbar, thus creating a visually busbarless string of shingled cells and, in turn, shingled modules.

Shingling leads to an increase in module output power density p_{out} because of the increase in active cell area and the low electrical resistance in the interconnection. The appealing homogeneous appearance raises interest in their use in vehicle-integrated PV (VIPV) and building-integrated PV (BIPV) applications. Even further increases in p_{out} can be achieved by using bifacial solar cells, which make use of the albedo light impinging from the rear side [16,17]. See Fraunhofer ISE's previous *Photovoltaics International* paper [24] for a discussion of shingling bifacial solar cells, such as bifacial passivated emitter and rear cells (PERC, biPERC) [18,19], passivated emitter, rear locally diffused (PERL) cells [20], passivated emitter and rear totally diffused (PERT) cells [21], heterojunction (HJT) cells [22], or TOPCon [23] cells.

The market shift towards PERC solar cells in the upcoming years [9] implies a shrinkage of the market share of aluminium back-surface field (Al-BSF) solar cells. The main shift in the market towards PERC solar cells is due to the clear advantages of the concept in terms of efficiency potential by having dielectrically passivated rear sides in comparison to the Al-BSF. PERC solar cells feature local contacts created by local contact openings (LCO) and subsequent metallization steps, which allows the PERC cell architecture to be designed for bifacial light collecting. This biPERC is obtained by replacing the full-area metallization on the rear side by a grid metallization that allows the harvesting of light from the rear side as well. Adapting the rear-side

"Shingling leads to an increase in module output power density because of the increase in active cell area and the low electrical resistance in the interconnection."

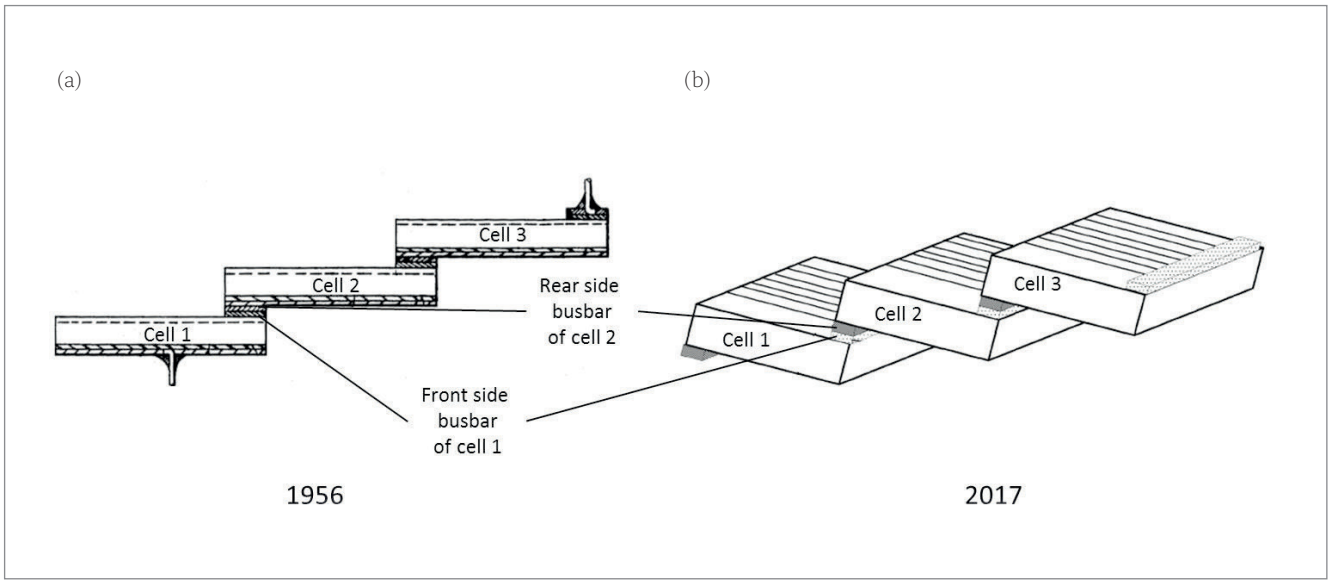

Figure 1. (a) Schematic showing a string of three shingled cells, adapted and labelled from an earlier 1956 patent [2]. (b) Schematic showing a string of three shingled cells in a recent 2017 patent (adapted and labelled) [11]. The similarities in (a) and (b) show the clear revival of the concept of shingling presented in both patent sketches. In cell shingling, the front and rear busbars of two neighbouring cells form the electrical and mechanical interconnection of two neighbouring cells.

passivation layers boosts the light coupling from the rear side. Although the concept of shingling can be applied to different cell architectures such as PERC, HJT, TOPCon and others (as explained in Wöhrle et al. [24]), the main focus in this paper is PERC-based shingle cells fabricated from 6" Czochralski-grown (Cz-Si) wafers, which are then integrated in the shingled module.

In the first part of this paper, Fraunhofer ISE's current fabrication process is presented, along with the characterization results for bifacial p-type shingled passivated edge, emitter and rear (pSPEER) solar cells [25] ready for shingled-module integration. The laser-assisted separation processes used for the fabrication of shingle cells are also described. Further investigation of the separated edge quality by modelling, simulations and photoluminescence (PL) measurements of the edge is discussed. In addition, Fraunhofer ISE's Passivated Edge Technology (PET), a post-metallization/separation edge passivation concept, is introduced. In the second part, as an essential step towards cell interconnection, available testing methods, along with the crucial properties of electrically conductive adhesives (ECAs), are presented. The paper also compares possible shingling design topologies and suggests numerous applications shown in demonstrated products, such as a PV-integrated car roof.

pSPEER solar cell concept and process

To obtain a bifacial shingle pSPEER cell, only one additional process step is needed compared with a large-area cell: the laser-assisted separation process. This separation process is preferably done after the back-end processes of the 6" host wafer have been completed (typically after firing). As reported in Baliozian et al. [25], pSPEER solar cells can be fabricated by just modifying the back-end processes. Other than the additional separation process step, the fabrication also requires the adjustment of the metallization layouts in order to obtain several shingle cells from each host wafer. In other words, PERC precursors (with deposited passivation layers) from an industrial production line can be used, and shingle cells of desired sizes can be manufactured. A specific fabrication batch of pSPEER cells using precursors is discussed later.

Current–voltage measurement of pSPEER cells

Rapid and precise current–voltage (I–V) measurements are a prerequisite for the characterization of shingle solar cells. The grid geometry, especially the adversely placed rear-side grid and the small cell size, poses new challenges for the I–V measurement set-up. Conventional measurement units with contacting pins are feasible for R&D purposes.

One option for measuring the cells is the use of inlays in the shape of conventional wafers, as shown in Fig. 2(a). The pSPEER cells are placed in the inlays and then electrically contacted by two I–V pin array strips on each of the front- and rear-side busbars, as shown in Fig. 2(b). Two additional arrays (one on each side) are used for mechanical stability purposes and therefore not electrically connected. To ensure the validity of the measurements, the I–V tester is calibrated with pSPEER cells measured at Fraunhofer ISE CalLab PV Cells. As a result of the measurement, a total area measurement (including the busbars) is obtained. Since the busbars are intended to be covered after interconnection, the efficiency of the area excluding the busbar area, or *designated area,* is of interest. Such designated area results can be obtained by subtracting the busbar area from the total cell area to determine the designated area short-circuit

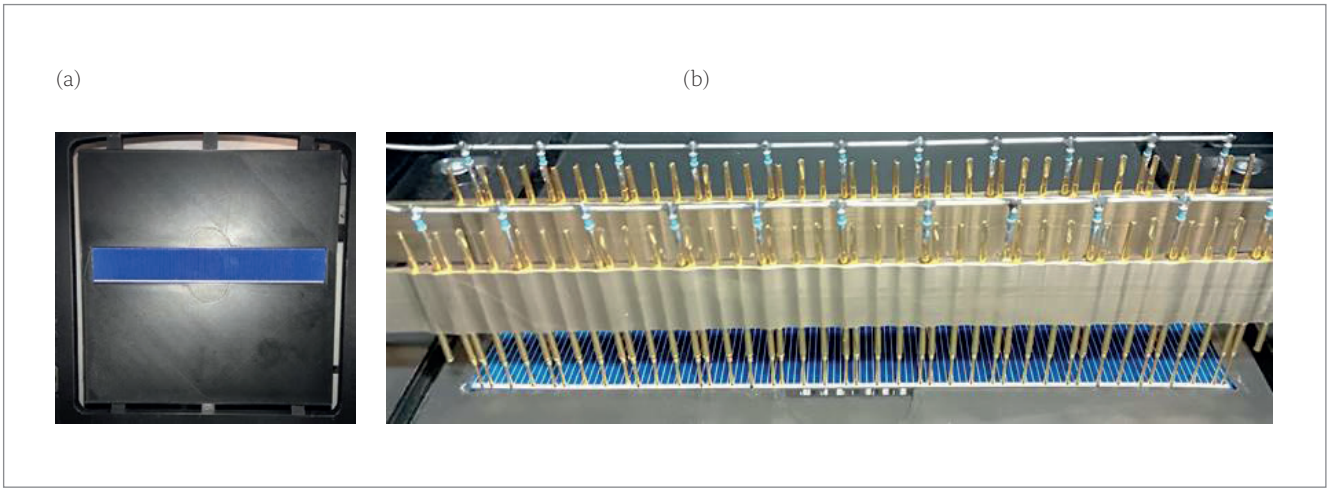

Figure 2. (a) Photograph of an inlay for pSPEER cells, which allows the use of a conventional *I–V* measurement unit. In this set-up, the pSPEER cell can be measured by two contacting *I–V* pin arrays that electrically contact the front and rear busbars. (b) Photograph of a front-side busbar contacted by the *I–V* pin array.

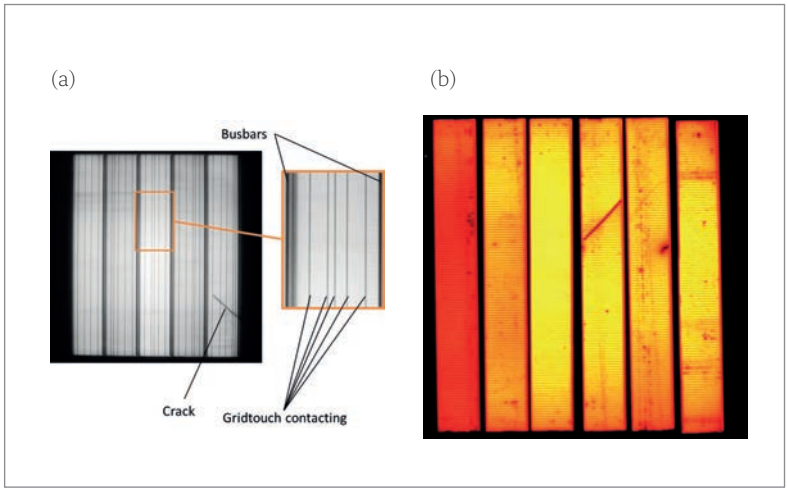

Figure 3. (a) Inline EL image of a finished host wafer before separation, contacted by a GridTOUCH unit. A microcrack can be identified in the lower right part of the cell, which would lead to a rejection of this pSPEER cell strip after separation. (b) PL image of separated pSPEER cells (not the same cell as in (a)). The PL image can uncover additional damage induced by the laser-assisted separation step; this covers edge-related flaws as well as new cracks or the like due to the additional handling. With a feasible automation system, multiple pSPEER cells could be measured simultaneously, making the procedure fast enough for inline characterization.

current density $j_{sc,des}$.

For a production line this set-up is suboptimal, as the throughput in terms of equivalent measured cell power scales down with the shingle size. Consequently, alternative approaches for measuring the efficiency of shingled cells are being investigated. The goal is to measure the cells on the host wafer with the conventional technique before the laser separation of the cell strips. Since the front and rear busbars are placed in an alternating pattern, the host wafers cannot simply be contacted with pin arrays like a conventional cell with busbars. GridTOUCH technology, with an orientation parallel to the busbars, is therefore preferred (see Fig. 3(a)). With this method, the efficiency information about the bundle of six yet to be separated shingles can be determined. Local information can be obtained by forward dark electroluminescence (EL), a common capability of today's *I–V* testers.

"Laser separation might introduce edge cracks, or even shunts, which also need to be inspected."

Laser separation, however, might introduce edge cracks, or even shunts, which also need to be inspected. One available option is to make use of inline contactless PL technology immediately after separation in order to detect flawed cells. Because of the wide field of view of the PL camera and the short measurement intervals of contactless measurements, several shingle cells can be measured simultaneously (assuming suitable automated handling of shingle cells), thus avoiding the previously mentioned throughput bottleneck. Fig. 3(b) shows a sample PL image of the measurement of six separated pSPEER cells.

pSPEER solar cell batch

The latest results for pSPEER cells are published in Baliozian et al. [26]. For this specific batch, industrial pre-processed precursors that feature a phosphorus-doped emitter passivated by a silicon nitride (SiN_x) layer were used (see Fig. 4(a)). The rear side is coated by a typical aluminium oxide (AlO_x) and SiN_x stack. The base resistivity of samples from a comparable batch is measured to be in the range $0.3\Omega cm \leq \rho_B \leq 0.9\Omega cm$.

The processing begins with laser LCO, carried out at Fraunhofer ISE by means of an infrared laser process. The external rear-side contacts, silver in this case, also known as the rear-side busbars, are first screen printed (the external silver contacts are analogous to the printed rear-side pads of 6" PERC cells). The rear-side aluminium grid is then applied, covering the LCO; this results in a silver busbar which is confined between aluminium grid contacts (see Fig. 4(b)). Next, the front-side silver contact grid is printed, and contact firing is performed in an industrial fast-firing oven. Six pSPEER cells of dimensions 22mm × 148mm are obtained after the laser scribing and mechanical cleaving separation

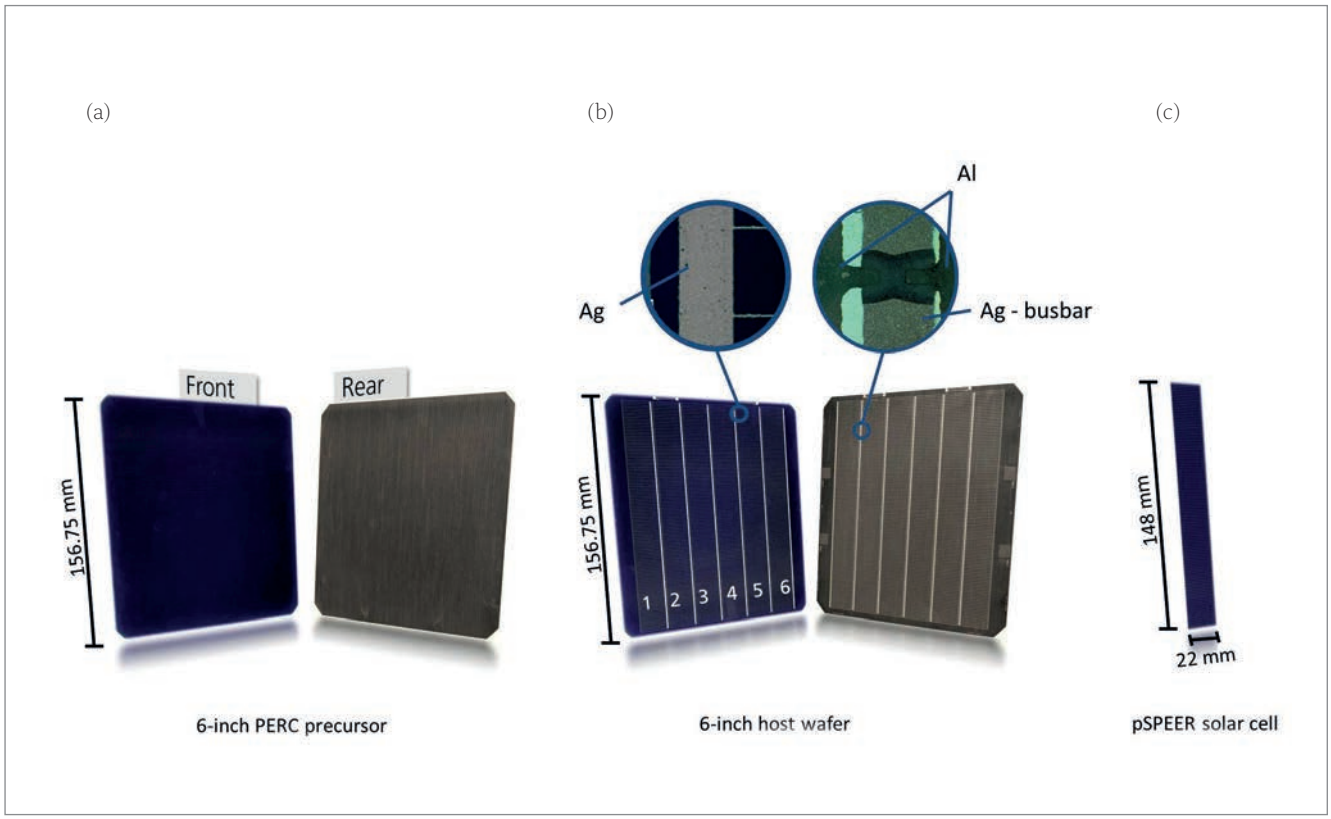

Figure 4. Scanned images of the front and rear sides of: (a) 6" industrial PERC precursor; (b) host wafer with front- and rear-metallization layouts (the microscope images show the metal contacts); (c) pSPEER solar cell of dimensions 22mm × 148mm. The precursors are not optimized for bifacial use, which explains the yellowish colour of the rear side.

process (see Fig. 4(c)). Such pSPEER cell dimensions are chosen to be utilized for research purposes because of the flexibility they offer when different industrial wafer formats are used.

For the characterization of the fabricated pSPEER cell, the measurements are taken at standard testing conditions (STC; G_r = 1,000W/m^2). As reported in Baliozian et al. [26], for the specific pSPEER cell with a nominal size 22mm × 148mm, *I–V* measurements show a peak designated area front-side efficiency of η_f = 21.4%, as shown in Table 1. The pSPEER cell yields an open-circuit voltage V_{oc} = 666mV, a fill factor *FF* = 79.8%, a pseudo-fill factor *pFF* = 82.3%, and a short-circuit current density $j_{sc,des}$ = 40.2mA/cm^2. The measurement of the same cell's rear side, also at STC, results in a designated-area rear-side efficiency η_r = 13.7%, featuring V_{oc} = 654mV, *FF* = 79.7% and $j_{sc,des}$ = 26.2mA/cm^2. Consequently, a bifaciality factor $\beta = \eta_r/\eta_f$ = 0.64 is determined. The pSPEER cell achieves a designated total output power density p_{out} = 22.8mW/cm^2 (calculated by considering an additional rear-side illumination with an irradiance G_r = 100W/m^2).

In the case of this particular cell, the rear-side $j_{sc,des}$ is $\Delta j_{sc,des}$ = 14mA/cm^2 lower than that of the front side; this difference is due to the high metallization fraction of the rear side compared with that of the front. Additionally, the optical properties of the rear side of the specific precursors utilized are not optimal, as they have not been adjusted for bifacial use. The difference in V_{oc} between the rear- and front-side measurements, or ΔV_{oc}, is ~12mV; this difference is due to the lower rear-side $j_{sc,des}$ and, to a lesser extent, to edge recombination, verified using the one-diode model equation.

On the other hand, the difference in *pFF* between a 6" bifacial PERC cell fabricated in a parallel batch and the separated pSPEER cell, or ΔpFF, is ~1.2%$_{abs}$; this shows the effect of edge recombination as a result of the separation process. As a by-product of the separation process, the edges are sparingly passivated with a thin native silicon oxide layer with no planned additional edge passivation process. To enhance the performance of the separated cell, an additional edge passivation process is therefore needed. The approach taken to decrease edge recombination by the selected

	η [%]	V_{oc} [mV]	$j_{sc,des}$ [mA/cm^2]	*FF* [%]	*pFF* [%]	β [1]
Front side	21.4	666	40.2	79.8	82.3	0.64
Rear side	13.7	654	26.2	79.7	81.6	

Table 1. *I–V* data for the pSPEER solar cell with the highest output power density p_{out} [26]. The designated area short-circuit current density values are obtained by subtracting the busbar area from the total measured cell area A_{tot} = 3,263mm^2.

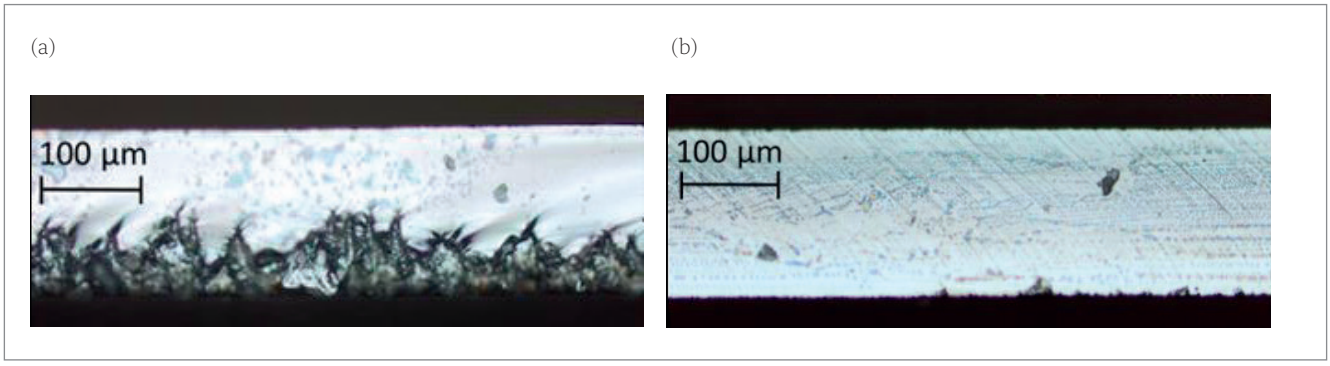

Figure 5. Microscopy images of pSPEER cell edges obtained by laser-assisted separation processes: (a) LSMC and (b) TLS [32].

laser-assisted separation process, as well as an additional edge passivation process, is discussed in upcoming sections.

Laser-assisted separation techniques and characterization

The most common way of separating shingle cells is to do a laser scribe followed by a mechanical cleave (LSMC). The laser scribe makes use of a pulsed laser to ablate the silicon along the entire separation path; the resulting laser perforation then enables an effortless separation by mechanical cleaving. The laser ablation, however, leads to melting and restructuring of the silicon in the cut region, resulting in an optically visible rough surface, as seen in Fig. 5(a). The destruction of the crystalline structure leads to a high number of defects at the edge. Since the shingle cells obtained have a high perimeter-to-area ratio, the damaged edges lead to significant losses.

Thermal laser separation (TLS) [27,28] is a gentle, kerfless alternative to LSMC separation. A short scribe beginning at the wafer edge is conducted by an infrared laser to initiate a crack. Subsequently, a continuous wave infrared laser (TLS cleave laser), followed by a water- and air-cooling jet, is guided over the wafer surface. The heating followed by cooling leads to thermal stress in the material, resulting in a crack propagation from the initial crack along the guided path. The process results in a smooth shingle cell edge surface, as shown in Fig. 5(b).

The TLS process, shown schematically in Fig. 6(a), is highly dependent on a variety of process parameters, including the cleave laser power, the feed rate, and the distance between the laser spot and the cooling spot on the sample [29]. The cleave process can be monitored by infrared imaging, whereby an elliptical shape of the laser spot on the sample (see Fig. 6(b)) is displayed. Depending on the cleave parameters, the heat distribution on the sample, as well as the total dissipated heat, can be optimized in order to achieve smooth separation edges and a straight separation path.

Since the TLS process does not lead to melting of the silicon but rather to cracking, this method is expected to cause fewer crystal defects and hence lower electrical losses. Almost no ablation takes place during TLS (only in the short initial scribe), which makes it an almost dust-free process. This is particularly attractive for high-throughput industrial applications [29,30]. Additionally, TLS-separated cells are mechanically more stable than LSMC-separated cells [31].

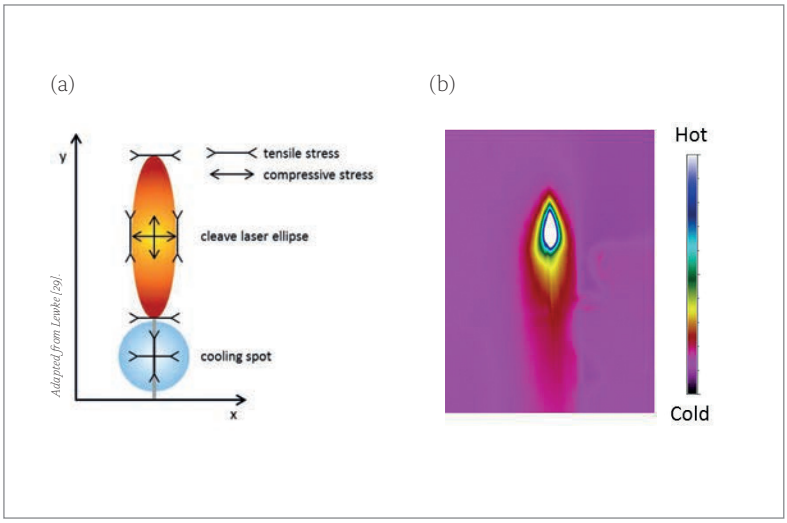

Figure 6. (a) Schematic of the TLS process. After a short laser scribe on the edge of the wafer to initiate a crack, a continuous-wave infrared laser is used to induce heat, directly followed by a water- and air-cooling jet; this leads to thermal stress and cracking of the substrate. (b) Infrared image displaying the heat profile on the substrate resulting from the laser followed by the cooling spot. The shape and size of the elliptical laser spot influence the TLS cut quality.

Model updates in the simulation tool Quokka3

The silicon solar cell modelling tool Quokka3 [33] has a dedicated extension for dealing with shingled cell technology, in order to improve the speed of modelling strip cells. It uses the recently integrated 'multidomain modelling', which can combine two or more simulation domains for modelling large-area devices while maintaining a small calculation mesh [34]. Solar cells with edge effects, half cells and shingled solar cell designs can be modelled using this approach.

A pSPEER cell is simulated with a core domain and one edge domain, as depicted in Fig. 7. The effective symmetry elements have the size of just the finger pitch multiplied by the finger length (approximately 1.3mm × 25mm) instead of half

the strip cell (approximately 25mm × 150mm) as performed in previous publications [35]. This reduces the simulation time from several hours to just a few minutes for each *I–V* curve. The edge domain features surface recombination models for the space charge and the bulk region, which can be addressed with the recombination parameters $j_{01,edge}$ or $S_{eff,edge}$ and $j_{02,edge}$. The integration of emitter windows along the edge with adjustable sheet resistances and surface recombination is also enabled.

Analytical model for edge recombination

In addition to having an excellent numerical modelling option for shingle cells, a simplified analytical model is useful for calculating the recombination at the edge of the solar cell; for details see Saint-Cast et al. [36]. The edges can be distinguished as linear recombination centres either close to or at the p-n junction; this is in contrast to local recombination on the rear surface (e.g. rear-contact recombination), where the recombination is mainly limited by the diffusion of minority carriers through the wafer from the front to the rear.

If it is assumed that translation along the axis of the defect in the system does not vary, it is possible to reduce the number of dimensions of the system to two. Another assumption is that the linear defect is the only source of inhomogeneity in this system. The high recombination rate at the edge (compared with the rest of the cell) induces a lower p-n junction potential difference (or a lower excess carrier density) in its proximity. The gradient of this potential leads to a flow of electrons and holes towards the defect – we are dealing with a carrier transport problem. In this model it is assumed (hypothesis 1) that over small distances (>1mm) relative to the size of the device (>1cm), the flow of the lateral carriers will be limited by resistive losses. In order to simplify this problem even further, it is assumed (hypothesis 2) that the vertical transport in the emitter and the bulk is small compared with the lateral transport, and can be modelled by simple sheet resistances (ρ_e for the emitter and ρ_B for the bulk).

Fig. 8 shows a schematic of the problem in three dimensions and a comparison with the developed model; the 3D problem is reduced to a single dimension as a result of the above-mentioned assumptions. The origin of the *x* axis is defined to be the location of the linear defect (edge). The local potential difference $V(x)$ at the p-n junction is calculated analytically.

Under open-circuit conditions, the p-n junction voltage decreases towards the edge because of the recombination at the edge. In Fig. 9, the p-n junction voltage is plotted as a function of position for six different illumination intensities. The 1 sun illumination intensity is defined for the sun spectrum AM1.5G at a power density of 1,000W/m^2. In this case an equivalent generation is achieved by monochromatic illumination at 808nm with a photon flux density $j_\gamma = 2.5 \times 10^{17}$cm^{-2}s^{-1} by illuminating

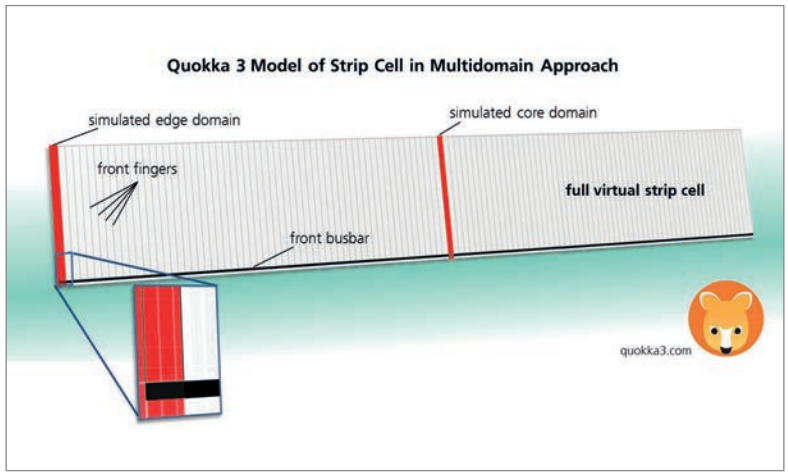

Figure 7. Schematic of the implementation of Quokka3's multidomain approach for a strip cell. The red front and core parts symbolize the two domains that are actually simulated. The greyed areas result from the cell's symmetry and do not need to be simulated in addition. This way, the duration of the simulation is greatly reduced.

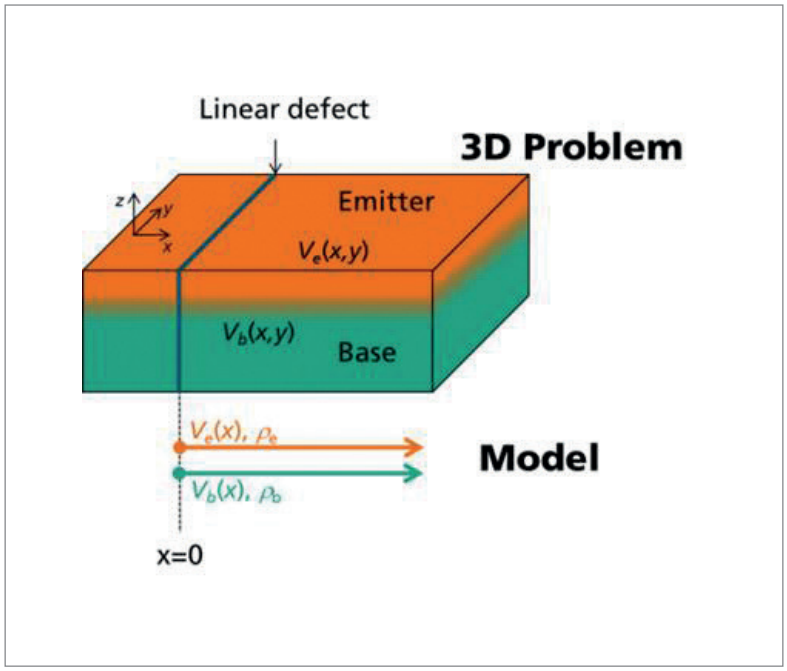

Adapted from Saint-Cast et al. [36]

Figure 8. Schematic of the problem in three dimensions, and a comparison with a simplified interpretation of a linear defect in a solar cell.

a reference solar cell of thickness $W \approx 160\mu$m at a temperature $T = 300$K. For low illumination, the p-n junction voltage is affected by the edge over a much greater distance than for high illumination. The results of the models were compared with 2D drift-diffusion simulations using Quokka3, and found to be in good agreement, within a deviation of ±3mV. For this example, the recombination parameter at the edge is $j_{02edge} = 19$nA/cm, which corresponds to a 'worst-case' value as identified by Fell et al. [37].

The benefit of such a model is the simplification of the analysis of measured cell parameters,

"A simplified analytical model is useful for calculating the recombination at the edge of the solar cell."

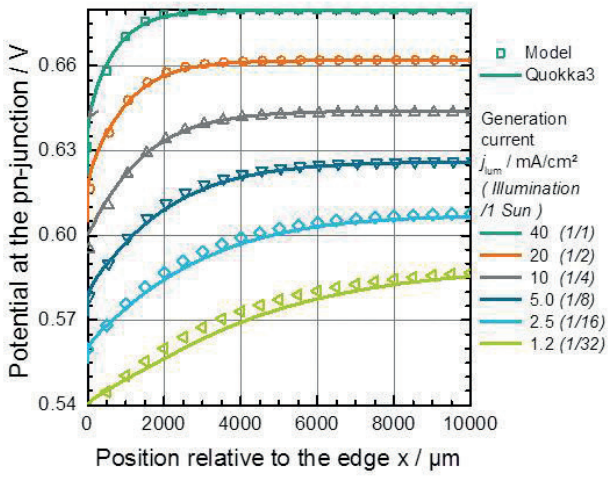

Figure 9. Potential difference at the p-n junction as a function of distance from the edge for different illumination intensities, with iV_{oc} = 680mV, $\rho_e + \rho_b$ = 180Ω/sq. and j_{02edge} = 19nA/cm.

which allows one to determine the recombination parameters at the edge (see next section); it also helps in understanding the physical principles behind edge recombination. This assumed model, verified by numerical simulation, shows that the transport mechanism of the carrier which recombines at the edge is mainly resistive.

Edge recombination analysis using PL measurements

Because the impact of edge recombination has been seen in the *I–V* parameters of the finished cells and in the modelling, there is clearly a demand for suitable in-depth characterization of this type of recombination. With reference to the investigation in Stolzenburg et al. [38], a new approach is presented to quantify edge recombination by using PL measurements combined with Quokka3 device and luminescence modelling. The main focus is to determine and separate the contribution of the two relevant edge recombination losses, as also proposed in Wöhrle et al. [35]: 1) recombination at the bulk edge, described by an effective surface recombination velocity $S_{eff,edge}$; and 2) recombination at the p-n junction edge, described by an edge-length-specific non-ideal recombination parameter $j_{02,edge}$.

Boron-diffused and Al_2O_3/SiN_x surface passivated n-type float-zone silicon wafers (ρ_B = 1Ωcm) with three differently processed wafer edges are investigated. The wafer is separated by: 1) TLS through the emitter layer from the front side; 2) TLS with a distance d_{EW} of 300µm between the emitter and the edge (emitter window); and 3) diamond cutter scribing and subsequent manual mechanical cleaving through the emitter layer.

The PL image of the three different edge types is depicted in Fig. 10(a) at an illumination intensity of 0.02 suns. The corresponding PL profiles in Fig. 10(b) clearly show a decrease towards the edges and a distinction between the differently processed edges. As a result, the TLS-cleaved edge through the emitter is not as affected by edge recombination as the mechanically cleaved edge. Further, the expected positive influence of an emitter window [35,39] due to the missing conductivity of minority carriers through the emitter to the edge is also observed.

For the quantification of the edge recombination, data from 2D PL simulations using Quokka3 are fitted to the experimental PL data. For this, a lifetime calibration is performed [40] and subsequently a fit by varying the two free parameters $S_{eff,edge}$ and

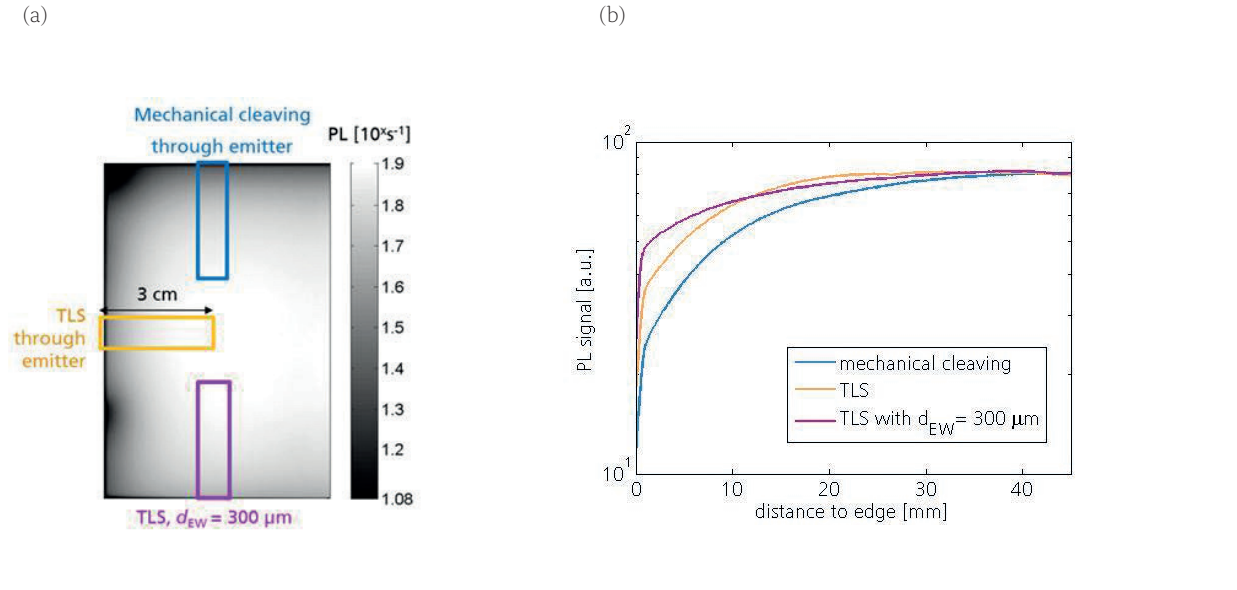

Figure 10. (a) Logarithmically scaled PL image at 0.02 suns, showing the three differently affected edges; (b) corresponding PL profiles averaged over the corresponding areas indicated by the coloured rectangles.

$j_{02,edge}$. A combined fit to six different illumination intensities (0.02 to 1 suns) allows the $S_{eff,edge}$ and $j_{02,edge}$ values to be distinguished. The best agreement between simulation and experiment for the TLS edge separated through the emitter is visible in Fig. 11, while the best-fit parameters for the investigated edges are listed in Table 2.

A comparison of these results with the worst-case assumption for an unpassivated edge proposed by Dicker [41] and Fell et al. [37] ($S_{eff,edge} \geq 10^6$cm/s and $j_{02,edge}$ = 13 or 19nA/cm, respectively) indicates that the values obtained in the present study are smaller, suggesting that some kind of native passivation is present on the edges. In particular, $j_{02,edge}$ is similar to the values given in the study by Rühle et al. [39], who also reported 5nA/cm for a mechanically cleaved unpassivated edge.

The method presented here can be used for extracting detailed information about the edge recombination. Since the overall goal is to optimize silicon solar cell performance, the comparison of mechanical cleaving and TLS leads to the conclusion that the TLS process causes lower edge losses and is therefore a promising separation method for shingle cells. Furthermore, the method is not constrained by specific sample parameters and can be employed for different high-efficiency silicon solar cells as well as for edge-passivated wafers in order to obtain detailed information about the edge recombination.

Post-metallization Passivated Edge Technology (PET)

Reports of some edge passivation approaches for reducing recombination at the edges can be found in previous studies. In one approach, for example, the formation of an emitter window by keeping the p-n junction a few hundred micrometres away from the separation edge reduces dangling bond recombination at the exposed space charge region [5,42]. Another approach is heavy doping of the entire separation path, creating an 'edge surface field', which induces the repulsion of carriers and reduces recombination at those intended regions [43]. Furthermore, a method proposing the generation of isolation trenches in the emitter also aims to reduce the flow of carriers towards the edges. An isolation trench can be realized by a laser ablation process, an additional wet-chemical etching and subsequent passivation of the trenches by, for example, thermally grown silicon oxide or polysilicon [44]. Although all these approaches lead to a reduction in edge recombination, the industrial feasibility is limited by the fact that the processes involved have to be performed at the front end, prior to metallization, and these processes can be numerous and perhaps costly.

It has also been reported that native silicon dioxide grown on chemically treated edges reduces perimeter recombination detected mainly in low-illumination conditions [45,46]. Moreover, the passivation of the p-n junction and/or the base directly at the edge by means of dielectric layers with high charge density has also been studied as a possible method for edge passivation [47]. However, the removal of damaged silicon induced by the separation process is seen to be necessary in order for a high-quality oxide passivation to form on the edge, as reported in Altermatt et al. [48].

> "The TLS process causes lower edge losses and is therefore a promising separation method for shingle cells."

On the other hand, a post-metallization/separation edge passivation method seems to be challenging: for this, an industrially feasible, or potentially feasible, edge passivation process is essential. A technical challenge is the stability of the metal contacts, which can degrade in post-firing thermal processes, as shown in Kontermann [49] and Chan et al. [50].

PET, developed at Fraunhofer ISE, aims to combine TLS separation, resulting in edges with less damage, with a high-quality edge passivation, without harming the solar cell contacts. The pSPEER cell that has undergone PET processing (pSPEER^{PET}) demonstrates an improved front-side designated area efficiency η_f = 22.1% and a total output power density p_{out} = 23.5mW/cm^2 (considering a rear-side irradiance G_r = 100W/m^2). Further details of these pSPEER^{PET} solar cells and the PET process can be found in Baliozian et al. [51].

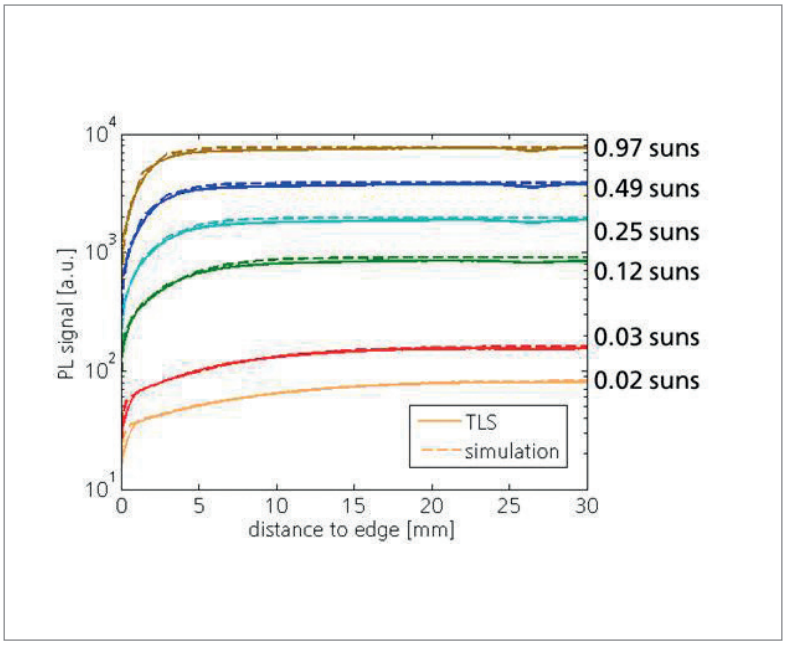

Figure 11. Comparison of the experimental and simulated data of the TLS edge using the best fit, which is shown for all six illumination intensities for the TLS edge with $j_{02,edge}$ = 3nA/cm and $S_{eff,edge}$ = 10^{5}cm/s.

Edges	$j_{02,edge}$ [nA/cm]	$S_{eff,edge}$ [cm/s]
TLS through emitter	3	10^5
TLS (d_{EW} = 300µm)	–	10^5
Mechanical cleaving through emitter	5	$\geq 10^6$

Table 2. Best-fit parameters for the three different unpassivated edge types.

Figure 12. A string of shingled solar cells produced by the TT1800 stringer, ready for module integration.

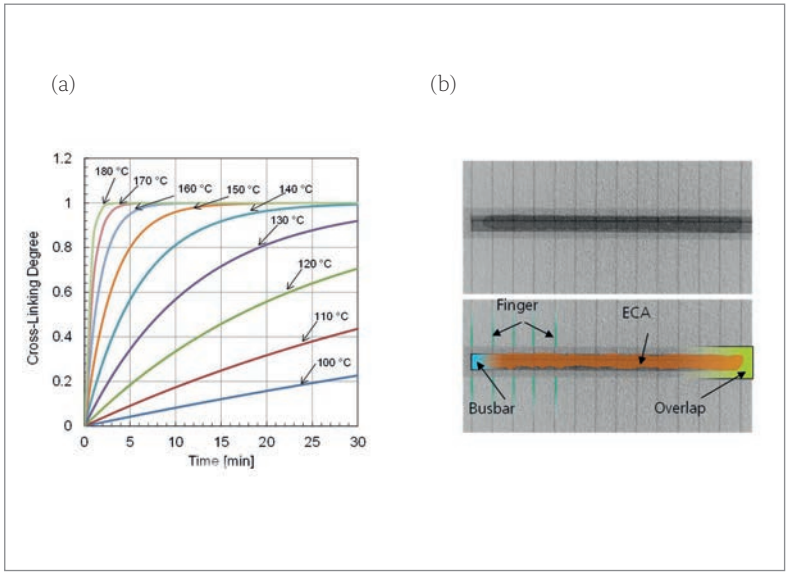

Figure 13. (a) Cure kinetics calculation derived from DSC measurements for an ECA, showing the cross-linking degree as a function of curing time and temperature. (b) X-ray transmission analysis of a shingle joint between neighbouring pSPEER cells (top image shows raw data; bottom image is shaded and labelled for better visibility).

Interconnection

In contrast to conventional solar modules, shingled-cell interconnection requires no ribbon or wire. Solar cells are interconnected directly within a small overlapping area, in a similar way to that of roof tiles. Such interconnection is realized in four steps:

1. Application of the ECA
2. Placement of the cells by a pick and place process
3. Curing (optional)
4. Lamination (with integrated curing)

The technologies for ECA application available at Fraunhofer ISE are dispensing, stencil printing and screen printing. On a lab scale, ECAs are either manually dispensed or applied using semiautomatic stencil and screen-printing processes. Additionally, a fully automated industrial-scale stringer (TT1800, developed in a joint cooperation with the stringer manufacturer teamtechnik) [52] is accessible for producing shingle strings of various lengths from cells of different sizes and geometries (see Fig. 12). Stencil and screen printing allow an arbitrary layout of the ECA in the joint and the optimization of ECA consumption. Furthermore, a robot-based pick and place process [53] allows the manufacturing of matrix shingle interconnection (discussed in more detail in the next section).

"The key element in shingling is the joint between the solar cells."

In contrast to soldering, ECAs interconnect the solar cells not by melting and solidifying but by a chemical cross-linking reaction, which is thermally activated; the reaction rate depends on temperature and typically starts at temperatures above 100°C. Curing durations can range from a few seconds to several minutes at temperatures of 150°C. This enables a combined lamination and curing process [54] as an alternative to an extra curing step before lay-up.

Since the key element in shingling is the joint between the solar cells, the module performance is highly dependent on the applied ECA; a thorough suitability assessment of ECAs is therefore crucial in order to ensure a reliable interconnection. A cure kinetics model based on differential scanning calorimetry (DSC) measurements has been developed [55] for specific optimizations of the temperature time profile in the stringing or lamination process to ensure a fully cured joint (see Fig. 13(a)).

Non-destructive X-ray transmission imaging yields information about the geometry and homogeneity of the manufactured joint with respect to cavities, even through the glass in the final laminate (see Fig. 13(b)). Destructive imaging methods include the fabrication of module cross sections after accelerated ageing tests in accordance with IEC 61215 [56], while optical methods, such as light microscopy and scanning electron microscopy (SEM), can be used to identify failure mechanisms inside the joint.

To support these experimental findings, structural–mechanical finite-element simulations allow a deeper understanding to be gained of the underlying effects in the joint when subjected to, for example, cycling temperatures or mechanical loads. Here, the characterization of the ECA bulk material with respect to its mechanical behaviour is an important input for the simulations.

Dynamic mechanical analysis (DMA) is performed to measure and model the viscoelastic properties of ECAs [57]. Fig. 14(a) shows typical DMA data of one material system used at Fraunhofer ISE to interconnect shingle solar cells. This specific material shows distinctive viscoelasticity between 40 and 120°C for frequencies ranging from 0.5 to 50Hz. Even though ECAs contain a high proportion of metal fillers to ensure electrical conductivity, the remaining organic binder matrix causes a viscoelastic behaviour.

By shifting these discrete sets of data via the use of the principle of time–temperature superposition, a master curve can be constructed (see Fig. 14(b)); this curve describes the relaxation spectrum of the material at a reference temperature, usually chosen to be the glass transition temperature T_g. Several rheological models exist that approximate such mechanical properties with spring-damper systems. A Comsol Multiphysics software implementation to carry out finite-element method (FEM) studies is performed by a fit of the data with the Generalized Maxwell Model [58]; a smooth representation of the data is achieved with i = 20 Maxwell arms. On the basis of this material modelling, FEM studies of the strings of shingled solar cells subjected to (thermo)mechanical loads have been carried out and published in Klasen et al. [57].

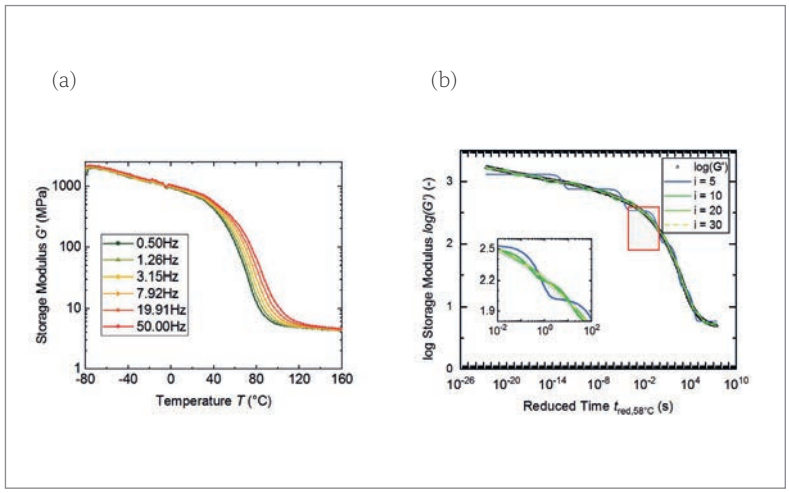

Figure 14. (a) Temperature-dependent stiffness of an ECA, measured at different excitation frequencies. (b) Corresponding master curve at T_g, derived from a shift of the data in the time domain and the use of the Generalized Maxwell Model to fit the data, with different numbers of Maxwell elements to achieve a smooth representation.

Module technology and application areas

The integration of solar cells into PV modules changes their output power because of optical and electrical effects. Absorption in module layers, reflection at optical interfaces, or resistive losses in solar cell interconnection are typical loss channels within a PV module.

In addition, when inactive module areas (e.g. cell spacing) are added, the geometrical reference area is increased. As a result, not only the output power of a cell but also the efficiency of the device is altered [59,60]. The cell-to-module (CTM) analysis, a methodology introduced by Haedrich et al. in 2014 [61], provides a versatile tool to assess these effects in module integration. Gains and losses are assigned to important module components (e.g. junction boxes, ribbons) and are shown as physical mechanisms, allowing the evaluation of module design and materials and the comparison of different module technologies.

The methodology provides a simple key figure to describe the success of module integration in terms of power or efficiency. The CTM ratio is the module power or efficiency divided by the initial cell power or efficiency; a ratio less than one represents a loss resulting from the integration of solar cells into the module, whereas a ratio greater than one indicates a gain.

Mittag et al. [62] have extended the CTM methodology to deal with shingled modules. All models are integrated into Fraunhofer ISE's SmartCalc.CTM software – a flexible, precise and user-friendly calculation tool for analysing CTM ratios for different module technologies (https://www.cell-to-module.com). Case studies performed with SmartCalc.CTM show that shingling technology significantly increases $CTM_{efficiency}$ ratios compared with conventional modules because of the elimination of cell spacing and interconnector shading.

In 2018 Fraunhofer ISE reintroduced the 'matrix shingle' topology, patented by Schmidt and Rasch

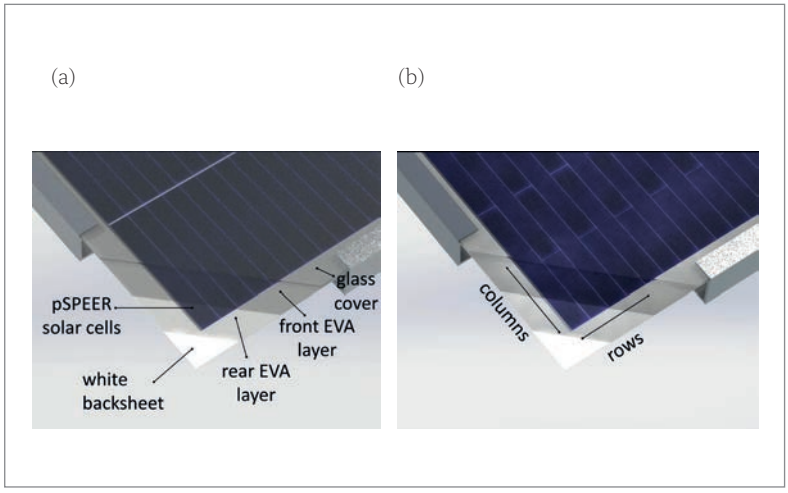

Figure 15. (a) Parallel string-based shingling topology, with string spacing. (b) Matrix-shingling topology, without inactive areas.

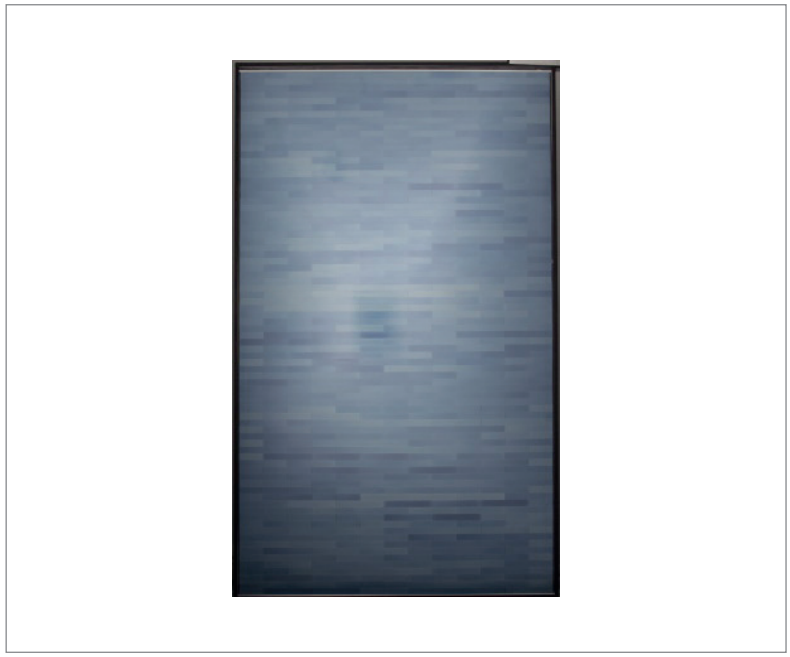

Figure 16. Top view of a bifacial matrix-shingled module (60-cell equivalent, rear side).

"The results of the CTM analysis show that matrix shingling is an effective approach for further increasing the module efficiency and power density of shingled modules."

in the early 90s [63]. Matrix shingling is a further improvement to string-based shingling and features increased cell packing and power density. As in string-based shingling (see Fig. 15(a)), matrix shingling entails the interconnection of cell rows in series by overlapping the solar cells vertically. Additionally, the cell strips of the subsequent cell row are shifted horizontally, resulting in a topology similar to that of a brick wall (see Fig. 15(b)). This means that within a single row the solar cells are connected in parallel via the overlapping front and rear busbars of horizontally adjacent cells. Because of the resulting series–parallel connection scheme, an improved module performance under partial shading conditions is achieved [15]. At the Intersolar Europe exhibition in 2018, Fraunhofer ISE demonstrated for the first time (to the authors' knowledge) a bifacial, matrix-shingled module in a 60-cell equivalent format (see Fig. 16).

To illustrate the potential of the matrix-shingling approach, a comparative CTM analysis was performed for a conventional string-shingled module and a matrix-shingled module. The matrix topology consists of 78 rows with six pSPEER solar cells in each row, while the string topology features six strings with 78 cells in each string. The cell power and the cell overlap are held constant for both topologies. The string design features a 2mm gap between neighbouring strings, whereas the matrix topology has no spacing. The module margins are kept the same; as a result, the matrix module can use a 1cm-smaller glass. Both modules incorporate a 3.2mm-thick glass with an anti-reflection coating, a 0.45mm-thick EVA encapsulant with a low UV cut-off, and a white TPT backsheet. The characteristics of the cells used are listed in Table 3, while the module topologies are summarized in Table 4.

The module power of the matrix-shingled module is found to be slightly less than that of the string-shingled design ($-2W_p$) because the gains from backsheet reflection in the string spacing areas are absent (compare k11 in Figs. 17 and 18). Since the matrix module is smaller and its cell packing is denser, the efficiency of the matrix topology is slightly increased in that design, with a power density improvement of $0.71W/m^2$ (+0.36%), as seen in Table 5.

The results of the CTM analysis show that matrix shingling is an effective approach for further increasing the module efficiency and power density of shingled modules. The benefit of the matrix approach becomes more relevant for bifacial modules with transparent back covers, when the reflection

gains from inactive spacing areas are not applicable.

The limited space availability on cars, planes or other vehicles require new approaches for module design. Matrix shingling is particularly interesting in the case of VIPV, where a high power density and enhanced performance under partial shading conditions is essential. In addition, a pleasing optical appearance with invisible solar cells is desirable in VIPV. Matrix shingling delivers a very uniform optical appearance by virtue of the absence of cell interconnector ribbons and cell or string spacing.

Unfortunately, solar cells usually have a dark appearance and lack the special look that some products require in terms of bright and brilliant colours. Fraunhofer ISE's bionic Morpho-Color® (a spectrally-selective photonic structure which replicates the same physical effect the morpho butterfly uses to achieve the brilliant optical appearance) fulfils that requirement and allows the customized design of PV modules with a wide choice of colours, but with a power loss of only $-7\%_{rel.}$ [64]. The combination of matrix shingling and Morpho-Color enables virtually invisible PV integration. To demonstrate the potential of this approach, a 2D curved matrix-shingled module with Morpho-Color coating was manufactured, demonstrating new possibilities for VIPV (see Fig. 19).

The high power density, the improved shading tolerance and the excellent aesthetics make matrix shingling highly suitable for integrated PV applications, such as BIPV or VIPV, as illustrated in Fig. 20. In an environment where high efficiencies, an attractive optical appearance and an excellent shading tolerance are essential, matrix shingling offers a very attractive solution.

Summary

The revival of the shingling concept for solar cells comes with a clear advantage potential in terms of an increase in the output power density p_{out} of modules. To achieve this goal, a number of challenges have to be tackled within the entire PV chain, from cell processing to module processing.

With an adaptation of the metallization layout and an advanced laser-assisted separation process, pSPEER solar cells can be fabricated in readiness for shingled-module integration. The laser-scribed and mechanically cleaved pSPEER solar cell yields a designated area front-side efficiency η_f = 21.4%, measured at STC. A total designated area output power density p_{out} = 22.8mW/cm^2 is achieved, when considering an additional rear-side irradiance G_r = 100W/m^2.

The recombination in the edge region is better understood by means of an analytical model, verified by numerical Quokka3 simulations. In addition, a PL-based method offers further insight into edge recombination. The method shows that the thermal laser separation process (through the emitter) leads to enhanced results in comparison to the diamond-cutter-scribed and mechanically cleaved edge separated through the emitter, quantified by the parameter $j_{o2,edge}$ = 3nA/cm.

At Fraunhofer ISE, a post-metallization/separation Passivated Edge Technology (PET) is under development, allowing higher cell efficiencies without compromising the stability of the metal contacts. A pSPEER cell processed with PET (pSPEER^{PET} solar cell) has achieved a designated η_f = 22.1% and p_{out} = 23.5mW/cm^2 (considering an additional G_r = 100W/m^2). The use of appropriate ECAs for the shingling interconnection, as well as a curing process, is necessary. The behaviour of the ECA material is seen to be viscoelastic.

The matrix-shingling topology demonstrates advantages with regard to superior aesthetics, thus making the approach attractive for integrated PV. A good example of the use of a matrix-shingled module is a vehicle-integrated roof module; the PV module is barely discernible, since the Morpho-Color glass surface integrates seamlessly into the car's structural form.

Acknowledgements

The work reported here was conducted within the framework of the PV-BAT 400 project (Contract No. 0324145), funded by the German Federal Ministry of Economics and Energy (BMWi). The authors would like to thank all their colleagues in the Fraunhofer ISE photovoltaic divisions for their contributions to advanced PV R&D.

References

[1] Chapin, D.M., Fuller, C.S. & Pearson, G.L. 1954, "A new silicon p-n junction photocell for converting solar radiation into electrical power", *J. Appl. Phys.*, Vol. 25, No. 5, p. 676.

[2] Dickson, J.D.C. 1960, "Photo-voltaic semiconductor

	pSPEER technology
Cell dimensions [mm^2]	156.75 × 22.00
Cell total area efficiency [%]	20.04
Cell power (STC) [W_p]	0.703
Ribbons	n/a

Table 3. Characteristics of the simulated cells used for both shingled-module concepts.

	String shingled	Matrix shingled
Number of cells	468	
Overlap [mm]	1.55	
String spacing [mm]	2	–
Top/bottom margins [mm]	36.7	
Side margins [mm]	18	
Glass format [mm]	3.2 × 1,667 × 987	3.2 × 1,667 × 977

Table 4. Topology characteristics for each shingled-module concept.

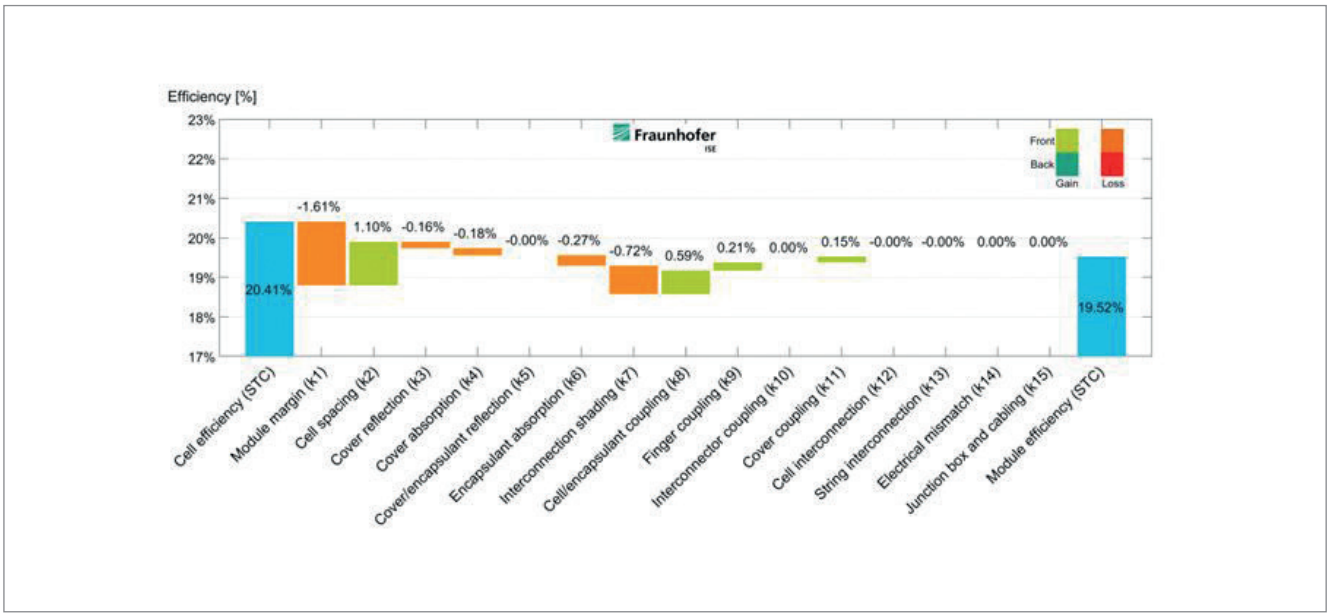

Figure 17. $CTM_{efficiency}$ diagram for the string-shingled module at STC.

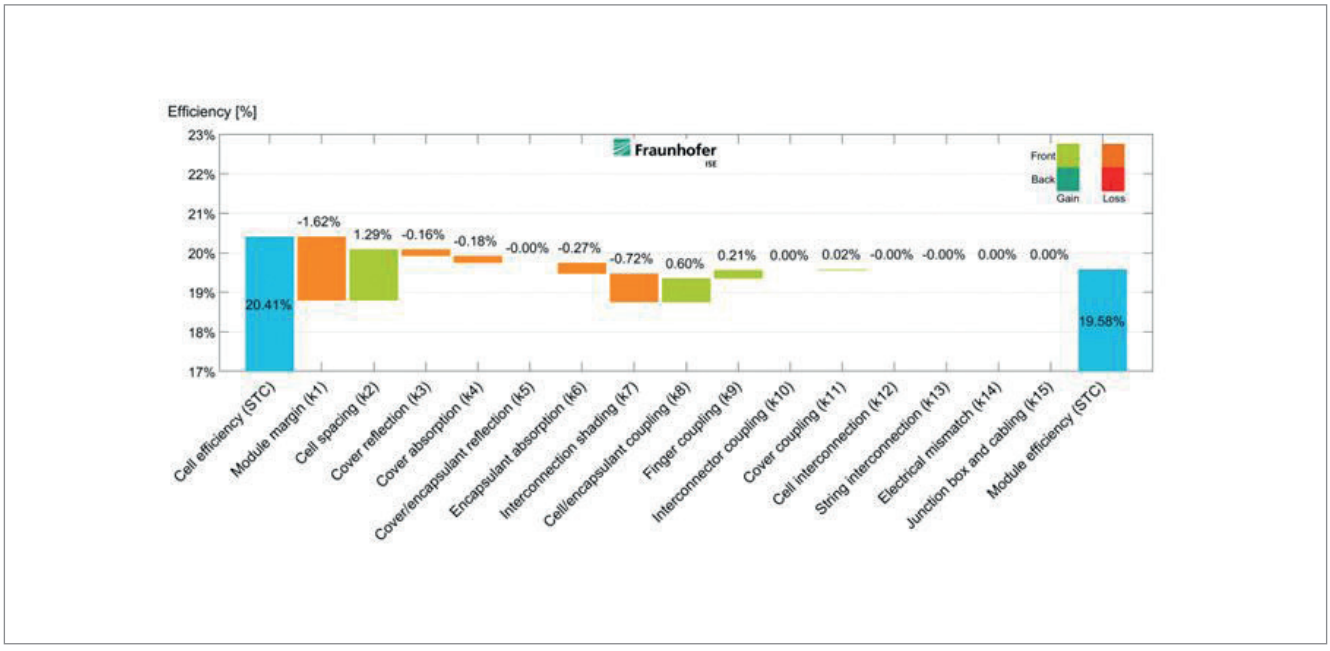

Figure 18. $CTM_{efficiency}$ diagram for the matrix-shingled module at STC.

	String shingled 1,667 × 987mm²	Matrix shingled 1,667 × 977mm²	$\Delta_{abs.}$
Cell input power [W_p]	329.49	329.49	0
Module power [W_p]	323.27	321.15	−2.12
Power density [W/m²]	196.48	197.19	+0.71
Module efficiency [%]	19.52	19.58	+0.06
CTM_{power} ratio [%]	98.11	97.47	−0.64
$CTM_{efficiency}$ ratio [%]	95.69	95.98	+0.29

Table 5. CTM analysis results for both shingled-module concepts.

apparatus or the like", US Patent 2,938,938.
[3] Nielsen, R.J. & Rongved, L. 1963, "Satellite solar cell assembly", US Patent 3,116,171.
[4] Leinkram, C.Z. & Oaks, W.D. 1973, "Shingled array of solar cells", US Patent 3,769,091.
[5] Glunz, S.W. et al. 2002, "High-efficiency silicon solar cells for low-illumination applications", *Proc. 29th IEEE PVSC*, New Orleans, Louisiana, USA, pp. 450–453.
[6] Zhao, J. et al. 1997, "20000 PERL silicon cells for the '1996 World Solar Challenge' solar car race", *Prog. Photovolt: Res. Appl.*, Vol. 5, No. 4, pp. 269–276.
[7] SunPower, "SunPower P-Series Solar Panel" [https://www.sunpower.de/sunpower-p-series-solar-panel].
[8] Canadian Solar Inc., "High density shingle modules" [https://www.canadiansolar.com/solar-panels/hidm.html].
[9] ITRPV 2019, "International technology roadmap

"The high power density, the improved shading tolerance and the excellent aesthetics make matrix shingling highly suitable for integrated PV applications."

Figure 19. Curved matrix-shingled car roof module presented at Intersolar 2019.

Figure 20. Illustration of an integrated PV-active car roof.

for photovoltaic (ITRPV): 2018 results", 10th edn (Mar.) [https://itrpv.vdma.org/en/].
[10] Morad, R. et al. 2015, "Shingled solar cell module", US Patent 2015/0349167 A1.
[11] Heng, J. et al. 2018, "Module fabrication of solar cells with low resistivity", Tesla Motors Patent 10,115,839.
[12] Tonini, D. et al. 2017, "Shingling technology for cell interconnection: Technological aspects and process integration", *Proc. 33rd EU PVSEC*, Amsterdam, The Netherlands.
[13] Rudolph, D. et al. 2017, "Cell design optimization for shingled modules", *Proc. 33rd EU PVSEC*, Amsterdam, The Netherlands.
[14] Schulte-Huxel, H. et al. 2019, "Interconnect-shingling: Maximizing the active module area with conventional module processes", *Proc. 9th SiliconPV*, Leuven, Belgium.
[15] Mondon, A. et al. 2018, "Comparison of layouts for shingled bifacial PV-modules in terms of power output, cell to module factor and bifaciality", *Proc. 35th EU PVSEC*, Brussels, Belgium.
[16] Luque, A. et al. 1984, "Diffusing reflectors for bifacial photovoltaic panels", *Solar Cells*, pp. 277–292.
[17] Kopecek, R. et al. 2015, "Bifaciality: One small step for technology, one giant leap for kWh cost reduction", *Photovoltaics International*, 26th edn.
[18] Blakers, A.W. et al. 1989, "22.8% efficient silicon solar cell", *Appl. Phys. Lett.*, Vol. 55, No. 13, pp. 1363–1365.
[19] Dullweber, T. et al. 2016, "PERC+: industrial PERC solar cells with rear Al grid enabling bifaciality and reduced Al paste consumption", *Prog. Photovolt: Res. Appl.*, No. 12, pp. 1487–1498.
[20] Lohmüller, E. et al. 2017, "Bifacial p-type silicon PERL solar cells with screen-printed pure silver metallization and 89% bifaciality", *Proc. 33rd EU PVSEC*, Amsterdam, The Netherlands.
[21] Meier, S. et al. 2017, "Fast co-diffusion process for bifacial n-type solar cells", *Solar RRL*, Vol. 1, No. 1.
[22] de Wolf, S. et al. 2012, "High-efficiency silicon heterojunction solar cells: A review", *Green*, Vol. 2, No. 1.
[23] Feldmann, F. et al. 2017, "Evaluation of TOPCon technology on large area solar cells", *Proc. 33rd EU PVSEC*, Amsterdam, The Netherlands.
[24] Wöhrle, N. et al. 2017, "Solar cell demand for bifacial and singulated-cell module architectures", *Photovoltaics International*, 36th edn, pp. 48–62.
[25] Baliozian, P. et al. 2018, "Bifacial p-type silicon shingle solar cells – the 'pSPEER' concept", *Solar RRL*.
[26] Baliozian, P. et al. 2018, "Bifacial pSPEER solar cells for shingle modules", *Proc. 35th EU PVSEC*, Brussels, Belgium, pp. 410–413.
[27] Lewke, D. et al. 2015, "Thermal laser separation – A novel dicing technology fulfilling the demands of volume manufacturing of 4H-SiC devices", *MSF*, Vol. 821–823, pp. 528–532.
[28] Röth, J. et al. 2015, "Thermal laser separation (TLS) dicing process study – A new technology for cutting silicon solar cells for high-efficiency half-cell modules", *Proc. 31st EU PVSEC*, Hamburg, Germany, pp. 716–718.
[29] Lewke, D. 2018, *Untersuchung und Minimierung lateraler Rissabweichungen beim Thermischen Laserstrahlreparieren*. Aachen: Shaker Verlag.
[30] Koitzsch, M. et al. 2013, "Improving electric behavior and simplifying production of Si-based diodes by using thermal laser separation", *Proc. 24th SEMI ASMC*, pp. 400–403.
[31] Eiternick, S. et al. 2014, "Loss analysis for laser

separated solar cells", *Energy Procedia,* Vol. 55, pp. 326–330.
[32] Baliozian, P. et al. 2018, "Bifacial shingle solar cells on p-type Cz-Si (pSPEER)", *Proc. 8th SiliconPV,* Lausanne, Switzerland.
[33] Fell, A. et al. 2017, "The concept of skins for silicon solar cell modeling", *Sol. Energy Mater. Sol. Cells,* Vol. 173, pp. 128–133.
[34] Fell, A. & Altermatt, P.P. 2019, "Detailed 3D full-cell modeling in Quokka3: Quantifying edge and solder-pad losses in an industrial PERC cell", *AIP Conf. Proc.,* Vol. 1999, No. 020007, pp. 1–5.
[35] Wöhrle, N. et al. 2017, "The SPEER solar cell Simulation study of shingled bifacial PERC technology based stripe cells.", *Proc. 33rd EU PVSEC,* Amsterdam, The Netherlands, pp. 844–848.
[36] Saint-Cast, P. et al. 2019, "Extracting metal and edge recombination parameters which are compatible with multi-dimensional cell simulations", *Proc. 36th EU PVSEC,* Marseille, France.
[37] Fell, A. et al. 2018, "Modeling edge recombination in silicon solar cells", *IEEE J. Photovolt.,* Vol. 8, No. 2, pp. 428–434.
[38] Stolzenburg, H. et al. 2019, "Edge recombination analysis of silicon solar cells using photoluminescence measurements", *Proc. 9th SiliconPV,* Leuven, Belgium.
[39] Ruhle, K. et al. 2015, "Impact of edge recombination in small-area solar cells with emitter windows", *IEEE J. Photovolt.,* Vol. 5, No. 4, pp. 1067–1073.
[40] Giesecke, J.A. et al. 2011, "Minority carrier lifetime imaging of silicon wafers calibrated by quasi-steady-state photoluminescence", *Sol. Energy Mater. Sol. Cells,* Vol. 95, No. 3, pp. 1011–1018.
[41] Dicker, J. 2003, "Analyse und Simulation von hocheffizienten Silizium-Solarzellenstrukturen für industrielle Fertigungstechniken", Dissertation, Faculty of Physics, University of Konstanz.
[42] Fellmeth, T. 2014, "Silicon solar cells for the application in low concentrator systems – Development and characterization", Dissertation, Faculty of Science, University of Tübingen.
[43] Mulligan, W.P. et al. 2000, "Development of chip-size silicon solar cells", *Proc. 28th IEEE PVSC,* Anchorage, Alaska, USA, pp. 158–163.
[44] Zhao, J. et al. 2000, "Peripheral loss reduction of high efficiency silicon solar cells by MOS gate passivation, by poly-Si filled grooves and by cell pattern design", *Prog. Photovolt: Res. Appl.,* pp. 201–210.
[45] Hermle, M. et al. 2003, "Analysis of edge recombination for high-efficiency solar cells at low illumination densities", *Proc. 3rd WCPEC,* Osaka, Japan, pp. 1009–1012.
[46] Dicker, J. 2003, "Analyse und Simulation von hocheffizienten Silizium-Solarzellenstrukturen für industrielle Fertigungstechniken", Dissertation, Faculty of Physics, University of Konstanz.
[47] Kuhn, R., Fath, P. & Bucher, E. 2000, "Effects of pn-junctions bordering on surfaces investigated by means of 2D-modeling", *Proc. 28th IEEE PVSC,* Anchorage, Alaska, USA, pp. 116–119.
[48] Altermatt, P.P., Heiser, G. & Green, M.A. 1996, "Numerical quantification and minimization of perimeter losses in high-efficiency silicon solar cells", *Prog. Photovolt: Res. Appl.,* Vol. 4, No. 5, pp. 355–367.
[49] Kontermann, S. 2009, "Characterization and modeling of contacting crystalline silicon solar cells", Dissertation, University of Konstanz.
[50] Chan, C. et al. 2017, "Instability of increased contact resistance in silicon solar cells following post-firing thermal processes", *Solar RRL,* Vol. 1, No. 11, 1700129 (1–5).
[51] Baliozian, P. et al. 2019, "Post-metallization 'Passivated Edge Technology' of separated bifacial shingle pSPEER solar cells", *IEEE J. Photovolt.* [submitted for publication].
[52] Fraunhofer ISE 2019, "Adhesive process developed for shingle cell technology", Press Release [https://www.ise.fraunhofer.de/de/presse-und-medien/presseinformationen/2019/klebeverfahren-fuer-schindeltechnologie-entwickelt.html].
[53] Klasen, N. et al. 2017, "Shingled cell interconnection: A new generation of bifacial PV-modules", *Proc. 7th Worksh. Metalliz. Interconn. Cryst. Sil. Sol. Cells,* Konstanz, Germany.
[54] Wirth, H. 2018, "Encapsulation form for a shingled photovoltaic module", WO 2018/087008 A1.
[55] Geipel, T. & Eitner, U. 2013, "Cure kinetics of electrically conductive adhesive", *Energy Procedia,* Vol. 38, pp. 340–347.
[56] IEC 61215-1-1, 2016, "Terrestrial photovoltaic (PV) modules – Design qualification and type approval – Part 1-1: Special requirements for testing of crystalline silicon photovoltaic (PV) modules.
[57] Klasen, N. et al. 2019, "FEM simulation of deformations in strings of shingled solar cells subjected to mechanical reliability testing", *Proc. 8th Worksh. Metalliz. Interconn. Cryst. Sil. Sol. Cells,* Konstanz, Germany.
[58] Ward, I.M. & Sweeney, J. 2013, *Mechanical Properties of Solid Polymers.* Chichester, UK: Wiley.
[59] Hädrich, I. 2014, "Unified methodology for determining CTM ratios: Systematic prediction of module power", *Proc. 4th SiliconPV,* 's-Hertogenbosch, The Netherlands.
[60] Pfreundt, A. et al. 2018, "Rapid calculation of the backsheet coupling gain using ray groups", *Proc. 35th EU PVSEC,* Brussels, Belgium.
[61] Haedrich, I. et al. 2014, "Unified methodology for determining CTM ratios: Systematic prediction of module power", *Sol. Energy Mater. Sol. Cells,* Vol. 131, pp. 14–23.
[62] Mittag, M. et al. 2017, "Cell-to-module (CTM) analysis for photovoltaic modules with shingled solar cells", *Proc. 44th IEEE PVSC,* Washington DC, USA.
[63] Schmidt, W. & Rasch, K.-D. 1990, "New interconnection technology for enhanced module efficiency", *IEEE Trans. Electron Dev.,* Vol. 37, No. 2, pp. 355–357.
[64] Bläsi, B. et al. 2017, "Morpho butterfly inspired coloured BIPV modules", *Proc. 33rd EU PVSEC,* Amsterdam, The Netherlands, pp. 2630–2634.

About the Authors

Puzant Baliozian received a B.Sc. in physics from the American University of Beirut in 2014, and an M.Sc. in renewable energy engineering and management from the University of Freiburg in 2016 for his thesis work completed at Fraunhofer IPM in the field of magnetocaloric energy conversion. He is currently a Ph.D. candidate at Fraunhofer ISE, and his main area of research is the development of p-type SPEER solar cells by focusing on the laser-assisted separation and edge passivation processes.

Nils Klasen studied chemical and process engineering at Karlsruhe Institute of Technology (KIT). He completed his master's thesis on large-area processing of perovskite solar cells at the Light Technology Institute (LTI) in 2015. In 2017 he began his Ph.D. studies within the module technology group of Fraunhofer ISE, and is focusing on the reliability of shingled cell interconnections.

Nico Wöhrle studied physics at the University of Freiburg, Germany, and received his diploma degree in 2012 for his work at Fraunhofer ISE on optical simulation of silicon solar cells. With a fellowship from the German Federal Environmental Foundation (DBU), he received his Ph.D. from the University of Freiburg in 2016 for his work on simulation of PERC solar cells. He is currently a researcher at Fraunhofer ISE, where he focuses on simulation and inline characterization of solar cells as well as on the conceptual development of p-type PERC solar cells.

Christoph Kutter obtained his B.Sc. in environmental engineering from the Hamburg University of Applied Sciences in 2015, for which he investigated the correlation between the LCOE of PV power plants and module design. In 2018 he received his M.Sc. in renewable energy engineering and management from the University of Freiburg for his thesis on the topic of CTM analysis of decorated integrated PV modules. As a scientist at Fraunhofer ISE, his current research focus is the development of module technology for integrated PV applications (BIPV, VIPV).

Hannah Stolzenburg studied physics at the University of Göttingen. She received her M.Sc. in 2018 with a focus on material and solid-state physics while spending one semester studying physics at the University of Ghent. For her master's thesis she investigated the interface between p-type silicon and aluminium oxide using deep-level transient spectroscopy. She is currently a Ph.D. student at Fraunhofer ISE, carrying out research on characterization and quantification of edge losses in silicon solar cells.

Anna Münzer received her B.Sc. in physics with a focus on semiconductor physics in 2015, after which she studied renewable energy engineering and management at the University of Freiburg. In 2018 she started working as an engineer at Fraunhofer ISE, where she is currently working on TLS process development in the research of shingled solar cells.

Pierre Saint-Cast received his M.Sc. and an engineering degree from the Polytechnic Institute of Grenoble in 2007. In 2012 he received his Ph.D. from the University of Konstanz, Germany. Since 2008 he has been with Fraunhofer ISE, where his research interests include the development of passivation layers for solar cell applications, especially PECVD of Al2O3 layers, and the analytical modelling of electrical transport in Si solar cells devices. He is currently the project manager and product manager for PERC solar cells at Fraunhofer ISE.

Max Mittag studied industrial engineering and management at the Freiberg University of Mining and Technology. In 2010 he completed his diploma thesis at Fraunhofer ISE and joined the PV module technology department. He is the head of the module efficiency team, and his current work includes CTM efficiency analysis, techno-economical assessments, and the development of new PV module concepts.

Elmar Lohmüller studied physics at the University of Tübingen, and at Nelson Mandela Metropolitan University, Port Elizabeth, South Africa. He received his diploma degree in 2010 for his work at Fraunhofer ISE on the development of p-type MWT-PERC solar cells, and then his Ph.D. from the University of Freiburg in 2015 for his work on the development of n-type MWT solar cells. He is currently a researcher at Fraunhofer ISE and focuses on the development of p-type PERC solar cells.

Tobias Fellmeth studied physics at the University of Konstanz, and received his diploma degree in 2009 for his work at Fraunhofer ISE on the development and characterization of MWT concentrator solar cells. He

subsequently received his Ph.D. from the University of Tübingen in 2014 for his work on silicon-based, low-concentrator solar cells. Currently a scientist and project manager at Fraunhofer ISE, he focuses on the development of bifacial PERC and TOPCon solar cells.

Mohammad Al-Akash was awarded his B.Sc. in energy engineering by the German Jordanian University. In 2019 he received his M.Sc. in renewable energy engineering and management from the University of Freiburg. His master's thesis focused on the evaluation of different post-metallization edge passivation methods of p-type SPEER solar cells.

Achim Kraft studied electrical engineering at the University of Applied Science in Hanover, and renewable energies at the University of Applied Science in Berlin. He obtained his master's in renewable energies before joining Fraunhofer ISE as a Ph.D. student in 2012. He received his Ph.D. in the field of plated copper front-side metallizations for silicon solar cells from the Albert Ludwig University of Freiburg, Germany, in 2015. Since then his research has focused on solar cell interconnection technologies and processes at Fraunhofer ISE, where he is head of the interconnection technologies team in the module research group.

Martin Heinrich completed his Ph.D. at the National University of Singapore in 2015, where he worked for two years at SERIS, and then for two years at Fraunhofer ISE. As a group leader at University of Freiburg, he focused on solar cell engineering and was the coordinator of the Solar Energy Engineering online study programme. In 2017 he joined the module technology department at Fraunhofer ISE and is the coordinator of the PV for Mobility programme.

Armin Richter received his Ph.D. in physics from the University of Konstanz, Germany, in 2014 for his work on n-type silicon solar cells with front-side boron-doped emitters and an in-depth characterization of aluminium-oxide-based silicon surface passivation. His current research interests include atomic layer deposition of functional thin films (e.g. passivation layers, electron/hole transport layers, TCOs) and in-depth characterization of dielectric surface passivation layers, as well as the development of high-efficiency silicon solar cells along the whole process chain and 3D device simulations.

Andreas Fell carried out his Ph.D. thesis work at Fraunhofer ISE, Germany, on the topic of modelling and simulation of laser processes for silicon solar cells. From 2011 to 2015 he was a research fellow at the Australian National University, where he developed laser processes and device simulation capabilities for silicon solar cells. In 2016 and 2017 he held a Marie-Curie fellowship position at Fraunhofer ISE, dedicated to developing the Quokka3 solar cell simulator and advancing solar cell modelling, which continues to be his research focus.

Alma Spribille, studied energy and environmental management at the European University of Flensburg, Germany. She completed work for her diploma thesis as an industrial engineer at Fraunhofer ISE, concerning MWT solar cells, in 2010, after which she joined the MWT Solar Cells & Printing Technology group. Since December 2017 she has been head of the Process Integration – Structuring and Metallization team.

Holger Neuhaus holds a Ph.D. from the University of New South Wales. He was a development engineer at Pacific Solar Pty Ltd, and then worked for more than 15 years at SolarWorld AG, where he was initially responsible for quality assurance and technology in cell production, and later headed the global R&D activities along the entire value chain. In 2018 he joined Fraunhofer ISE and is in charge of module technology.

Ralf Preu studied physics at the universities of Freiburg and Toronto, and economics at the University of Hagen, Germany. After being awarded a Ph.D. degree in electrical engineering, he joined Fraunhofer ISE in 1993 and has worked in different fields in PV, including system monitoring, silicon solar cell and module technology, characterization and simulation. He is the director of the PV Production Technology division at Fraunhofer ISE, where his main focus is R&D of advanced silicon solar cell technology and its transfer to industrial production. He also teaches photovoltaics at the University of Freiburg.

Enquiries
Puzant Baliozian
Fraunhofer Institute for Solar Energy Systems ISE
Heidenhofstraße 2
79110 Freiburg, Germany

Tel: +49 (0)761 4588 5383
Email: puzant.baliozian@ise.fraunhofer.de